Fine structure of defects in radial nematic droplets

S. Mkaddem*
UGRU, UAE University, Al-Ain, Abu Dhabi, United Arab Emirates

E. C. Gartland, Jr.†
Department of Mathematics and Computer Science, Kent State University, Kent, Ohio 44242
(Received 15 February 2000)

We investigate the structure of defects in nematic liquid crystals confined in spherical droplets and subject to radial strong anchoring. Equilibrium configurations of the order-parameter tensor field in a Landau–de Gennes free energy are numerically modeled using a finite-element package. Within the class of axially symmetric fields, we find three distinct solutions: the familiar radial hedgehog, the small ring (or loop) disclination predicted by Penzenstadler and Trebin, and a solution that consists of a short disclination line segment along the rotational symmetry axis terminating in isotropic end points. Phase and bifurcation diagrams are constructed to illustrate how the three competing configurations are related. They confirm that the transition from the hedgehog to the ring structure is first order. The third configuration is metastable (in our symmetry class) and forms an alternate solution branch bifurcating off the radial hedgehog branch at the temperature below which the hedgehog ceases to be metastable. Dependence on temperature, droplet size, and elastic constants is investigated, and comparisons with other studies are made.

PACS number(s): 61.30.Jf, 61.30.Gd, 64.70.Md

I. INTRODUCTION

The study of equilibrium structures and defects of confined liquid crystals has been an area of interest for some time. Here we consider the problem of spherical droplets of a nematic with radial strong-anchoring conditions modeled by a Landau–de Gennes tensor order-parameter model. We are motivated primarily by the succession of papers [1–4]. In [1] Schopohl and Sluckin illustrated for this problem the structure of a radial hedgehog configuration with an isotropic core. Penzenstadler and Trebin [2] then showed that the core should instead broaden to a small ring (or loop) disclination (of 180° or strength 1/2). This was validated numerically by Sonnet, Kilian, and Hess in [3] (using a tensor representation and iterative solution algorithm similar to [5]) and was also validated in [6] (using a lattice Monte Carlo model). Rosso and Virga [4] argued that the radial hedgehog solution remained at least metastable over a certain, broader range of parameters.

Several issues raised by these papers have motivated us in our present investigation. A prediction of the first-order nature of the transition from the hedgehog to the ring configuration is stated in [3]. Related to this is the analysis in [4] of the metastability limits of the hedgehog. In the latter paper (as well as in [2]), a certain approximation (constraint on the degree of order) was used, and the question arose as to what extent some of the conclusions of those papers might have been affected by the imposition of this assumption. These issues are clarified here where we explicitly delimit coexistence regions and metastability limits for the competing configurations. In addition, we examine how closely our calculated (unconstrained) solutions conform to the constraint of [2,4].

Another matter concerns the dependence of the phase boundaries on anisotropy of the elastic constants. The numerics in [3] (as well as [6]) considered only the equal-elastic-constants model; whereas Rosso and Virga [4] pay considerable attention to the changes in stability and structural phase behavior induced by varying the relative magnitudes of these constants. Here we use a general Landau model with two elastic constants—because of the strong-anchoring conditions and elastic-constant degeneracy of these models, this is the maximal number of independent constants that can be considered. We observe marked quantitative differences as the elastic constants are varied.

A final issue concerns the equilibrium radius of the disclination loop and how it depends on the model parameters. For large droplets, this should depend only on intrinsic parameters, and an indication of this is given in [3]. Penzenstadler and Trebin [2] perform an analysis that leads to a prediction of how the radius of the ring should depend on temperature and elastic constants. We explore this numerically and find qualitative agreement.

II. MODEL

A. Free energy and scalings

Consider a Landau–de Gennes expansion of the free energy in powers of the tensor order parameter $\mathbf{Q}$ and its gradient $\partial\mathbf{Q}=\{Q_{\alpha\beta,\gamma}\}$:

$$\mathcal{F}(\mathbf{Q}) := \int [f_e(\partial\mathbf{Q}) + f_b(\mathbf{Q})]\,dV,$$

where the elastic and bulk free-energy densities are given by

*Electronic address: smkaddem@uaeu.ac.ae
†Also affiliated with Chemical Physics Interdisciplinary Program, Liquid Crystal Institute, Kent State University, Kent, OH. Electronic address: gartland@mcs.kent.edu

$$f_e := \frac{L_1}{2} Q_{\alpha\beta,\gamma} Q_{\alpha\beta,\gamma} + \frac{L_2}{2} Q_{\alpha\beta,\beta} Q_{\alpha\gamma,\gamma}$$

and

$$f_b := \frac{A}{2}\mathrm{tr}(\mathbf{Q}^2) - \frac{B}{3}\mathrm{tr}(\mathbf{Q}^3) + \frac{C}{4}\mathrm{tr}(\mathbf{Q})^2.$$

We nondimensionalize this model in terms of the (fixed) length scale $\xi_0 := \sqrt{27CL_1/B^2} = \sqrt{L_1/A_{\mathrm{NI}}}$ (where $A_{\mathrm{NI}} := B^2/27C$ denotes the nematic-isotropic transition value for a homogeneous uniaxial bulk sample governed by f_b) and rescaled variables

$$\tilde{\mathbf{r}} := \frac{\mathbf{r}}{\xi_0}, \quad \tilde{\mathbf{Q}} := \sqrt{\frac{27C^2}{2B^2}}\mathbf{Q}, \quad \tilde{\mathcal{F}} := \sqrt{\frac{27C^3}{4B^2L_1^3}}\mathcal{F}.$$

In terms of these (after dropping the tildes), the densities take the form

$$f_e = \frac{1}{2} Q_{\alpha\beta,\gamma} Q_{\alpha\beta,\gamma} + \frac{\eta}{2} Q_{\alpha\beta,\beta} Q_{\alpha\gamma,\gamma}$$

and

$$f_b = \frac{t}{2}\mathrm{tr}(\mathbf{Q}^2) - \sqrt{6}\ \mathrm{tr}(\mathbf{Q}^2) + \frac{1}{2}\mathrm{tr}(\mathbf{Q}^2)^2,$$

where

$$\eta := \frac{L_2}{L_1}, \quad t := \frac{27AC}{B^2} = \frac{A}{A_{\mathrm{NI}}}.$$

The important dimensionless parameters, then, are the elastic-constant ratio η, reduced temperature t, and radius of the droplet in units of ξ_0, which we shall denote by R.

These units were chosen to permit easy comparison with [1–4]. The length scale ξ_0 is comparable to the length scales utilized in [1,3]; it corresponds to a (temperature independent) coherence length or nematic correlation length, at the nematic-isotropic transition temperature. For this interpretation to be completely valid, ξ_0 should depend as well on L_2 (see, for example, [7], Sec. 2.5), as is the case in [1] and [2], Eq. (15); we have chosen the definition of ξ_0 above for convenience.

In terms of t, the critical values in the bulk are $t=0$ (''pseudocritical temperature,'' below which the isotropic phase is unstable), $t=1$ (nematic-isotropic transition temperature or ''clearing point''), and $t=\frac{9}{8}$ (''superheating limit,'' above which the ordered phase does not exist). Thus one unit of our reduced temperature roughly corresponds to the width of the coexistence range for the nematic and isotropic phases of the material in the bulk, which is around 1–2 °C for typical low-molecular-weight liquid crystals. In order for the elastic free-energy density to be positive definite, it is necessary that

$$0 < L_1, \quad 0 < 3L_1 + 5L_2,$$

or

TABLE I. Experimental material constants of MBBA. T_c is the clearing point T_{NI}, T_c^* is the pseudocritical point or supercooling limit T_{SC}, $A = a(T - T_c^*)$, K_{11}, K_{22}, and K_{33} are the Frank elastic constants at $T = 25\,^\circ$C.

Constant	Value
a[a]	0.42×10^3 J/m^3 °C
B[a]	0.64×10^4 J/m^3
C[a]	0.35×10^4 J/m^3
L_1[a]	0.61×10^{-11} J/m
K_{11}[c]	0.6×10^{-11} J/m
K_{22}[c]	0.4×10^{-11} J/m
K_{33}[c]	0.75×10^{-11} J/m
L_2/L_1[b]	$\leqslant 1.6/(1.45\pm0.4)$
T_c[c]	46 °C
$T_c - T_c^*$[a]	1 °C

[a]E. B. Priestley, P. J. Wojtowicz, and P. Sheng, *Introduction to Liquid Crystals* (Plenum, New York, 1975), p. 168, Table 1.
[b]T. W. Stinson and J. D. Litser, Phys. Rev. Lett. **30**, 688 (1973).
[c]L. M. Blinov and V. G. Chigrinov, *Electro-optic Effects in Liquid Crystal Materials* (Springer, New York, 1994), p. xiv, Table I.

$$-\tfrac{3}{5} < \eta \tag{1}$$

(see [8,9]).

As a point of reference, we give in Table I the relevant experimental material parameters for MBBA, which we take as a representative low-molecular-weight liquid crystal. From these data, we obtain a nematic correlation length (at the clearing point) of

$$\xi_0 = \sqrt{\frac{27CL_1}{B^2}} \simeq 1.186\times10^{-7}\ \mathrm{m} \approx 120\ \mathrm{nm}$$

and a reduced temperature of

$$t = \frac{27AC}{B^2} = \frac{27aC}{B^2}(T - T_c^*) \simeq 0.97(T - 45).$$

Here $A = a(T - T_c^*)$, with T in °C and $T_c^* = 45\,^\circ$C, the experimental pseudocritical point for MBBA. In theory, we should have the relationship $B^2/27aC = T_c - T_c^*$; so this agrees well with the experimentally determined value of $T_c - T_c^* = 1\,^\circ$C. Thus we can simply think of t as the number of degrees above or below the pseudocritical temperature for the given material (here, above or below 45 °C for MBBA). Our rescaling of the order parameter for this material gives

$$\tilde{\mathbf{Q}} = \sqrt{\frac{27C^2}{2B^2}}\mathbf{Q} \simeq 2.01\mathbf{Q}.$$

Thus for MBBA our order-parameter values are roughly doubled.

One can compare such a Landau model to the Frank elastic model, under the assumption of uniaxiality

$$\mathbf{Q} = S(\hat{\mathbf{n}} \otimes \hat{\mathbf{n}} - \tfrac{1}{3}\mathbf{I}),$$

to obtain the relations

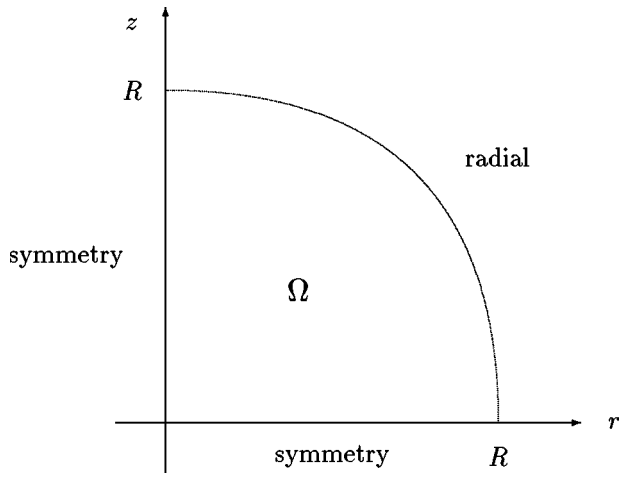

FIG. 1. Computational domain and boundary conditions.

$$K_{11}=K_{33}=(2L_1+L_2)S^2 \quad \text{and} \quad K_{22}=2L_1S^2.$$

This illustrates the well-known elastic-constant degeneracy of the model and leads to two slightly different experimental values for $\eta(=L_2/L_1)$ for MBBA:

$$\eta=2\left(\frac{K_{11}}{K_{22}}-1\right)=1.0 \quad \text{or} \quad \eta=2\left(\frac{K_{33}}{K_{22}}-1\right)=1.75.$$

The elastic constant L_2 is difficult to determine, and this material does not conform exactly to the condition $K_{11}=K_{33}$. Taking into account the reported experimental upper bound on L_2/L_1 in Table I, we take reasonable values for η for this material to be in the range $1.0\leqslant\eta\leqslant 1.5$.

B. Symmetry reduction

Our initial objective was to compare the hedgehog and ring-disclination solutions. Both of these possess high degrees of symmetry, which we use to reduce the domain for the calculations as well as the number of degrees of freedom in the tensor order-parameter field.

1. Geometry

The radial hedgehog configuration is completely spherically symmetric; while the ring disclination is axially symmetric. In addition, the ring solution (as well as the hedgehog) possesses a reflection symmetry across the plane perpendicular to its rotational symmetry axis. We take the z axis to be the rotational-symmetry axis and the x-y plane to be the mirror-symmetry plane, and we thus reduce our geometric domain to the quarter circle depicted in Fig. 1. We will use cylindrical coordinates (r, θ, z) and give below appropriate symmetry boundary conditions for the $r=0$ and $z=0$ boundaries of the domain.

2. Tensor representation

The tensor order parameter $\mathbf{Q}$ normally possesses five degrees of freedom: it is a symmetric, traceless, second-rank tensor. However, the particular configurations we seek are such that the $\mathbf{Q}$ tensor always has an eigenvector in the direction $\hat{\mathbf{e}}_\theta$ (normal to the r-z plane). This enables us to represent $\mathbf{Q}$ at each point in terms of just three degrees of freedom. For this purpose, we have found it convenient to utilize the formalism of [5] (see also [3]) and use the representation

$$\mathbf{Q}(r,z)=q_1(r,z)\mathbf{E}_1+q_2(r,z)\mathbf{E}_2+q_3(r,z)\mathbf{E}_3, \tag{2}$$

where

$$\mathbf{E}_1:=\frac{1}{\sqrt{6}}\begin{bmatrix}-1&0&0\\0&-1&0\\0&0&2\end{bmatrix}, \quad \mathbf{E}_2:=\frac{1}{\sqrt{2}}\begin{bmatrix}1&0&0\\0&-1&0\\0&0&0\end{bmatrix},$$

and

$$\mathbf{E}_3:=\frac{1}{\sqrt{2}}\begin{bmatrix}0&0&1\\0&0&0\\1&0&0\end{bmatrix}.$$

Here the normalization is chosen so that these basis tensors satisfy the orthogonality condition

$$\mathrm{tr}(\mathbf{E}_i\mathbf{E}_j)=\delta_{ij},$$

which helps to simplify some of the formulas.

After integrating with respect to θ, we obtain a free energy of the form

$$F(\mathbf{q})=4\pi\int_\Omega [f_e(\mathbf{q},\nabla\mathbf{q})+f_b(\mathbf{q})]r\,dr\,dz.$$

The expressions for the densities above (in cylindrical coordinates) are somewhat complicated and are presented in Appendix A.

C. Boundary conditions

We impose a radial strong-anchoring condition on the outer boundary, requiring the $\mathbf{Q}$ tensor to be uniaxial with a degree of order (scalar order parameter) equal to the bulk equilibrium value:

$$\mathbf{Q}=\sqrt{\tfrac{3}{2}}\,S_0(\hat{\mathbf{e}}_r\otimes\hat{\mathbf{e}}_r-\tfrac{1}{3}\,\mathbf{I}) \quad \text{on} \quad r^2+z^2=R^2, \tag{3}$$

with

$$S_0(t)=\frac{3+\sqrt{9-8t}}{4}. \tag{4}$$

This is translated into conditions on the scalar degrees of freedom q_1, q_2, and q_3 in Appendix B.

Mirror symmetry across the x-y plane implies the conditions

$$q_{1,z}=q_{2,z}=q_3=0 \quad \text{on} \quad z=0.$$

Rotational symmetry around the z axis implies

$$q_{1,r}=q_2=q_{2,r}=q_3=0 \quad \text{on} \quad r=0.$$

The coordinate-system-induced singularity at $r=0$ gives rise to this larger number of conditions there.

The numerical finite-element package we utilize below takes the problem input in its weak formulation (variational form, weak/integral form of the Euler-Lagrange equations),

as opposed to the strong formulation of the equilibrium conditions (as a Euler-Lagrange system of partial differential equations). In such a situation, it is necessary to specify only the essential boundary conditions to be satisfied by the trial functions, which for our problem are

$$q_3 = 0, \quad \text{on } z = 0$$

and

$$q_2 = q_3 = 0 \quad \text{on } r = 0.$$

We see that symmetry demands that the eigenframe of the **Q** tensor align with the $\hat{\mathbf{e}}_r$-$\hat{\mathbf{e}}_\theta$-$\hat{\mathbf{e}}_z$ coordinate frame along the r axis; while **Q** is required to be uniaxial along the z axis with director in the direction of $\hat{\mathbf{e}}_z$ [its scalar order parameter being given along this axis by the values of $S(z) := q_1(0,z)$].

III. NUMERICAL APPROACH

The strong form of the equilibrium conditions (Euler-Lagrange equations) consists of a coupled system of three nonlinear elliptic partial differential equations in the unknown scalar fields $q_i(r,z)$, $i = 1,2,3$. The nonlinearity is mild (involving only undifferentiated terms in the differential equations), and the equations are singular along $r = 0$ (due to the coordinate system). There exist modern software packages capable of solving such problems in general, and we have utilized two of them: parallel ELLPACK (//ELLPACK) [10] and the VECFEM library [11].

//ELLPACK is a prototype of a domain specific problem solving environment for elliptic and parabolic partial differential equations and systems. It contains a wide array of tools for the input of problems (in a high-level specification syntax), generation of grids and meshes, discretizations, solvers, visualization, and postprocessing. In the future, much of the type of numerical modeling in which we have engaged here will be performed with the aid of such environments. More information can be obtained from the references in [10] and from [12].

VECFEM is a FORTRAN library of discretizations and solvers for finite-element analysis of nonlinear elliptic and parabolic partial differential equations and systems. It is less comprehensive in its functionality than //ELLPACK—in which it is in fact contained as a submodule—but it is quite powerful for the problems within its scope. It requires as input a finite-element mesh, user-coded subroutines to define the problem (partial differential equations in weak formulation, essential boundary conditions), parameter choices and settings (tolerances, types of elements, array sizes, etc.), and an initial guess. It returns an equilibrium solution, which may or may not be locally stable (or metastable), calculated to user-specified stopping tolerances. In addition, it contains modules for the evaluation of auxiliary functionals on the calculated solutions, eigensolvers for associated eigenvalue problems, and *a posteriori* local error estimators. For more information see [11] or [13].

For our application, in addition to computing equilibrium solutions, we require their free energies (in order to determine the globally stable solution and to generate phase diagrams) and also the minimum eigenvalue of the second variation of the free energy (to determine if a computed solution is metastable or not). For these analyses, we were able to use the auxiliary functionals and eigensolvers of the VECFEM library.

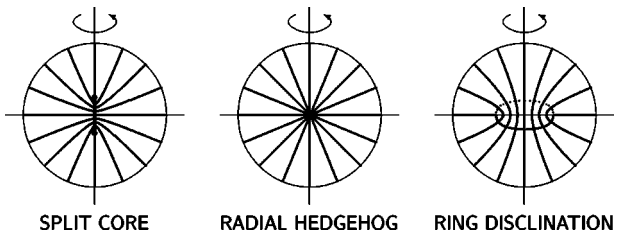

FIG. 2. Qualitative features of three axially symmetric equilibrium director profiles in a radially aligned spherical nematic droplet.

The accurate determination of phase boundaries for this problem requires highly accurate values of the free energies, and this motivated us to use high-order finite elements, type-2 triangular elements. In addition to conforming better to the curved part of the boundary, they give more accurate solution fields and free energies with fewer total triangles and degrees of freedom than the traditional type-1 triangular elements—the asymptotic error is fourth order versus second in the mesh size (see, for example, [14]).

For typical runs, we have used 64 triangles per edge (manually graded to be denser near the origin) giving a total of 4096 triangles, 8385 nodes (six nodes per triangle), and 24 385 unknowns (three unknowns per node). From a crude initial guess, it can take a few minutes on our workstation to converge; in continuation mode (where parameters are being changed slightly and good initial guesses are available), the convergence is faster. In the ''nice'' parameter ranges (modest R, around 20–25 units, say, and t close to zero), the accuracy of the computed fields is about 10^{-3} to 10^{-4}; while the accuracy of the associated free energies and minimum eigenvalues is 10^{-6} to 10^{-7}. This deteriorates as R increases and/or t becomes more negative, and some indications of this can be detected in the extremities of some of our graphics.

IV. NUMERICAL RESULTS

A. Configurations

Within this model and symmetry class, we find three distinct configurations: the familiar radial hedgehog, the ring disclination of Penzenstadler and Trebin [2], and a solution that we refer to as the split-core configuration (consistent with [15]). A qualitative rendering of the director fields of these three solutions is given in Fig. 2.

The radial hedgehog is the most familiar. It is completely spherically symmetric, everywhere uniaxial with a director in the radial direction, and possesses an isotropic core. We give a rendering of one of our calculated hedgehogs in Fig. 3. The order-parameter tensor field is visualized as a field of rectangular boxes (similar to [3], here down-sampled from the actual calculated field) aligned with the eigenframe of the **Q** tensor with axes scaled in proportion to $(2\lambda_i + \Lambda)/3\Lambda \in [0,1]$, where λ_i, $i = 1,2,3$, are the eigenvalues of the tensor at the point and Λ is a normalizing constant chosen so that $-\Lambda/2 \leqslant \lambda_i \leqslant \Lambda$. Adjacent is a plot of the three eigenvalues along the r axis. The degenerate (double, minimum) eigenvalues are visually indistinguishable, and the calculated solution is uniaxial to the level of our discretization error. The

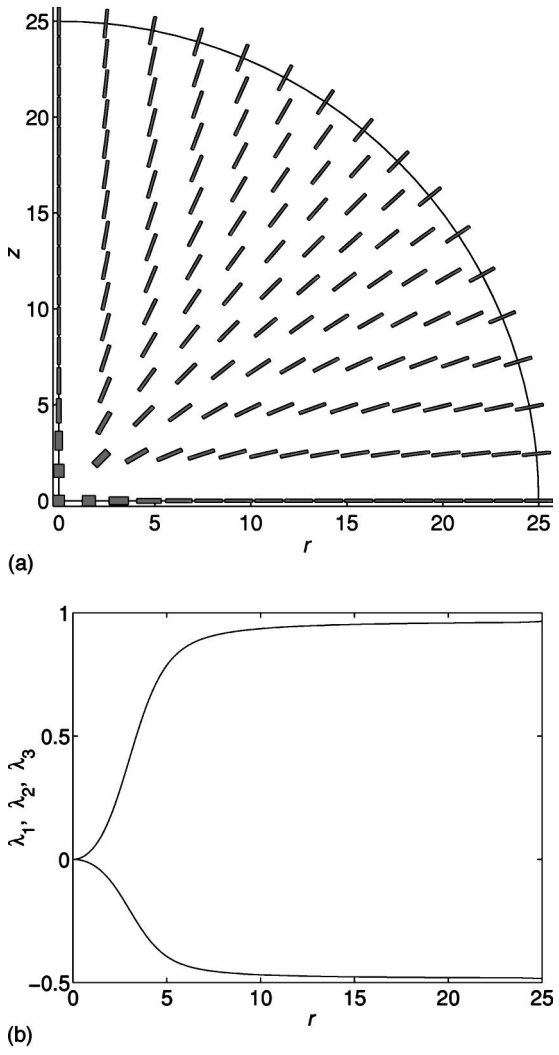

FIG. 3. Hedgehog tensor field and associated eigenvalues of Q tensor along r axis. Parameters: $\eta=0$, $t=0.75$, $R=25$.

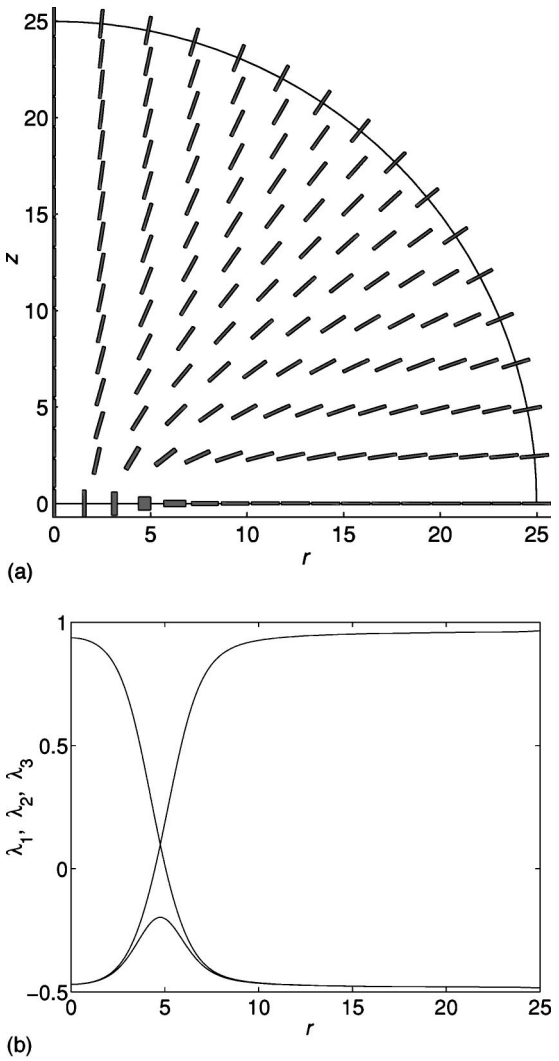

FIG. 4. Ring-disclination tensor field and associated eigenvalues of Q tensor along r axis. Parameters: $\eta=0$, $t=0.75$, $R=25$.

core structure and profile agree with those reported in [1] and [3].

Here (and in all of the figures) all lengths continue to be expressed in units of ξ_0 (the nematic correlation length at T_c), which for our reference material MBBA is roughly 120 nm. For this particular sequence of pictures, we also have taken $\eta=0$, which corresponds to $L_2=0$ (the equal-elastic-constants case $K_{11}=K_{22}=K_{33}$). Thus, for a low-molecular-weight liquid crystal with roughly equal elastic constants, this would correspond to a core size of approximately 0.5 μm for this temperature, which is in the coexistence region (in the bulk) and close to T_c.

In our normalization, a uniaxial tensor is written

$$\mathbf{Q}=\sqrt{\tfrac{3}{2}}\,S(\hat{\mathbf{n}}\otimes\hat{\mathbf{n}}-\tfrac{1}{3}\,\mathbf{I}),$$

where S is the scalar order parameter (degree of order) and $\hat{\mathbf{n}}$ is the director (unit eigenvector associated with the distinguished, nondegenerate, eigenvalue of $\mathbf{Q}$). This leads to the relations

$$\mathrm{tr}(\mathbf{Q}^2)=S^2$$

and

$$\lambda_{\max}=\sqrt{\tfrac{2}{3}}\,S$$

for the extremal eigenvalue of $\mathbf{Q}$. Thus in Fig. 3, with $t=0.75$, we have [from Eq. (4)]

$$S_0(0.75)=\frac{3+\sqrt{3}}{4}\simeq 1.183$$

and

$$\lambda_{\max}=\sqrt{\tfrac{2}{3}}S_0\simeq 0.966,$$

and we can see that this value is approached asymptotically just beyond the hedgehog core. As previously noted, these values are amplified by the rescaling of $\mathbf{Q}$. For MBBA (for which this scaling factor is roughly 2), this would correspond to a scalar order parameter (in the traditional scaling) of roughly 0.48.

The small ring disclination was first predicted by Penzenstadler and Trebin in [2]. It was numerically calculated for the equal-elastic-constants case in [3] (and in [6], using Monte Carlo simulation). It was further analyzed in [4]. We present a representative of our calculated results in Fig. 4.

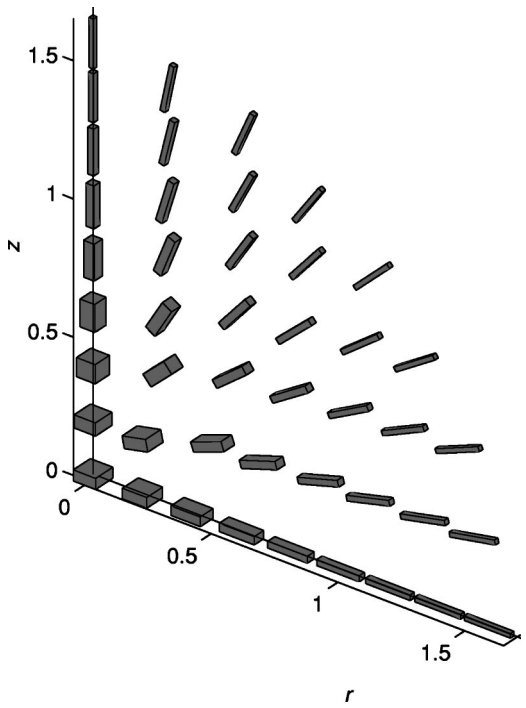

FIG. 5. Split-core (line disclination segment) tensor field (enlargement of inner region). Parameters: $\eta=0$, $t=-12$, $R=25$.

We see that the solution is effectively uniaxial away from the vicinity of the ring, where it goes through a local biaxial transition as the director reorients from the radial direction at the boundary to the vertical direction at the origin (without rotating the eigenframe of the **Q** tensor). The radius of the ring here (for this set of parameters) is roughly the same size ($5\xi_0$) as the hedgehog core in Fig. 3.

In [2], and also in [4], the pointwise constraint

$$\mathrm{tr}(\mathbf{Q}^2)=\lambda_1^2+\lambda_2^2+\lambda_3^2=-\frac{A}{C} \tag{5}$$

is imposed on the eigenvalues of the **Q** tensor—this value results from minimizing $A\,\mathrm{tr}(\mathbf{Q}^2)/2+C\,\mathrm{tr}(\mathbf{Q}^2)^2/4$ with respect to $\mathrm{tr}(\mathbf{Q}^2)$ (effectively treating the ''*B* term'' in f_b as a negligible perturbation). The effect of this on the eigenvalue profiles can be seen by comparing Fig. 4 here (where no such constraint is imposed) with Figs. 5 and 6 of [2], where the smallest eigenvalue is forced by the constraint to bow out and down.

The split-core configuration has not been previously reported to our knowledge. We render an enlargement of the inner area of this solution in Fig. 5. We have used a much lower temperature, $t=-12$, in order to obtain features of reasonable size. The configuration consists of a very short line disclination segment (of 360° or strength 1, a local planar radial or planar uniaxial structure) along the *z* axis (rotational symmetry axis) terminating in isotropic end points (the split remnants of the isotropic core of the hedgehog). The field of eigenvalues associated with this **Q** tensor field is a little more complicated than those of the other two configurations. Along the *z* axis, symmetry implies uniaxiality; whereas approaching the origin from any other direction, one observes local biaxiality. In Fig. 6, the eigenvalues are plotted for three different directions of approach.

B. Bifurcation and phase behavior

It is not immediately clear how these three solutions are related to each other. They can be seen to be topologically equivalent, in that any one can be continuously transformed into any other. Both the ring and the split-core solutions result from a breaking of the spherical symmetry of the hedgehog. The ring configuration results from a horizontal spreading of the hedgehog core into a disclination loop; while the split-core solution develops by splitting the core in the vertical direction to form a disclination line segment.

We have explored these numerically. Figure 7 gives a representative bifurcation diagram, which illustrates these transformations with respect to temperature changes. A convenient parameter to distinguish the three solutions is provided by their scalar order parameter at the origin $S(0)=q_1(0,0)$: all three configurations are uniaxial at the origin (by symmetry), with the ring being positively ordered in the vertical direction $[S(0)>0]$, the hedgehog isotropic $[S(0)=0]$, and the split core negatively ordered $[S(0)<0]$. In our bifurcation diagram, we plot this value on the vertical axis against the reduced temperature *t* along the horizontal axis. The similarity to the first-order nematic-isotropic transition in the (uniaxial) bulk is apparent.

The picture now becomes clear. As temperature is reduced, the hedgehog loses its metastability at a certain point (just before $t=-5$ for the parameters here), beyond which it

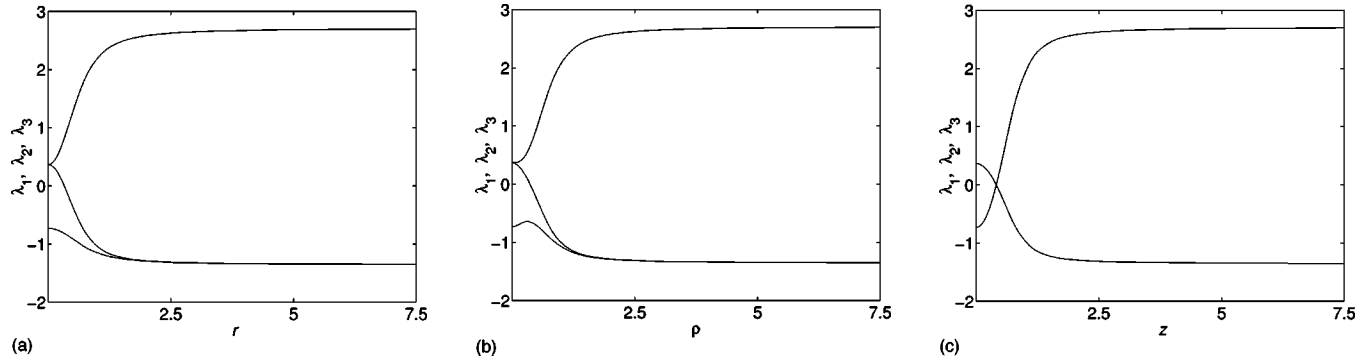

FIG. 6. Eigenvalues of *Q* tensor field for inner region of split-core (line disclination segment) configuration (Fig. 5) along *r* axis (left), along 45° ($r=z$) radial line (center), along *z* axis (right).

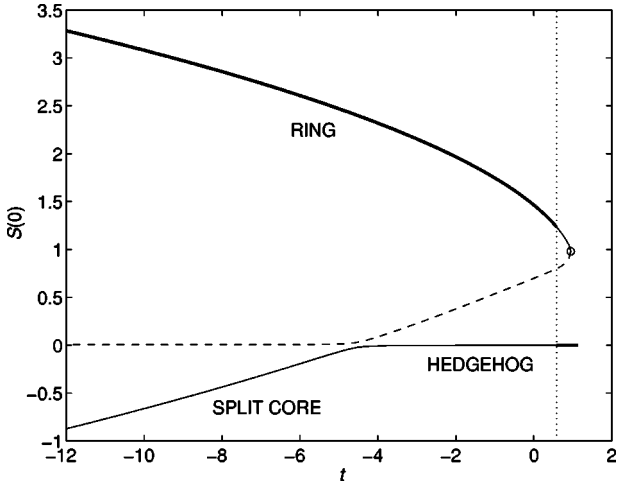

FIG. 7. Bifurcation diagram of discretized model for radial hedgehog, ring-disclination, and split-core solutions. Scalar order parameter at the origin $[S(0)]$ vs reduced temperature (t). Bold line indicates stable equilibrium (minimum free energy); solid line indicates metastable (locally stable); dashed line indicates not metastable (not locally stable). Parameters: $\eta=0$, $R=25$. Transition value: $t=0.583$. Ring limit/turning point: $t\simeq 0.947$.

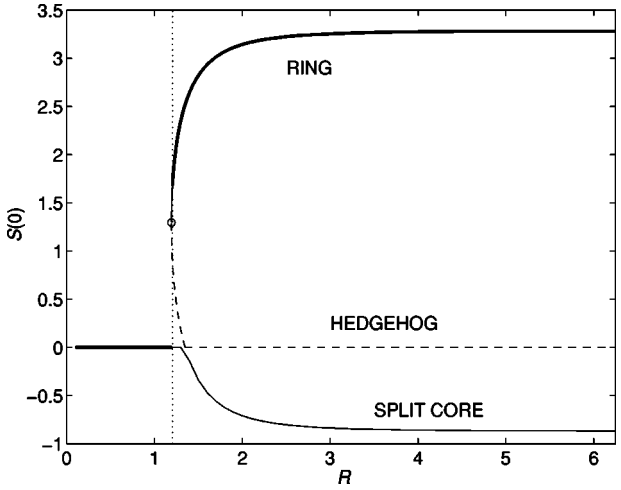

FIG. 8. Bifurcation diagram of discretized model for radial hedgehog, ring-disclination, and split-core solutions. Scalar order parameter at the origin $[S(0)]$ vs droplet radius (R in units of ξ_0). Bold line indicates stable equilibrium (minimum free energy); solid line indicates metastable (locally stable); dashed line indicates not metastable (not locally stable). Parameters: $\eta=0$, $t=-12$. Transition value: $R\simeq 1.206$. Ring limit/turning point: $R\simeq 1.193$.

continues to exist as a locally unstable equilibrium solution. Off this point bifurcates the branch that contains the other two solutions. The upper part of this branch corresponds to the ring solution, which is locally unstable until its radius becomes sufficiently large. The lower part is the split core, which is always metastable—at least within our symmetry class. The first-order transition from hedgehog to ring is fairly strong, with a coexistence region of almost $-5<t<1$. The simple bifurcation point (and branch crossing) has separated slightly under our discretization. This example of ''imperfect bifurcation'' is probably caused here by the fact that in such a finite-element model as ours, the symmetry boundary conditions that are ''natural'' (i.e., those that involve derivatives) are only weakly imposed and only approximately satisfied by the calculated fields; thus the discrete model adheres to the level of discretization error to this aspect only of the symmetry of the continuous problem. Motivated by these numerical results, we have constructed elsewhere an analytical argument proving that for such a model the hedgehog must become locally unstable at a sufficiently low temperature in a sufficiently large droplet [15].

The bifurcation can be similarly viewed as a transition with respect to R (for fixed t). This is done in Fig. 8, at a rather low temperature $t=-12$, where the branching has become very steep. It reveals similar features, with the hedgehog becoming locally unstable above a very small critical value of R. The bulk value of the scalar order parameter for this temperature is given [again using Eq. (4), with $t=-12$] by

$$S_0(-12)=\frac{3+\sqrt{105}}{4}\simeq 3.312,$$

and this value can be seen to be very quickly approached at the center of the droplet for the ring configuration.

Which configuration is stable (global free-energy minimizer) depends on the model parameters (here in dimensionless form) temperature t, droplet radius R, and elastic constants η. This dependence is explored numerically in [3] for the case of equal elastic constants ($\eta=0$, Fig. 7 of that paper). Here we have constructed similar phase diagrams, Figs. 9 and 10, that in addition take into account the effect of different elastic constants ($\eta\neq 0$) and also indicate the metastability limits of the solutions. The solid lines in these two figures demark the hedgehog-to-ring transition. For our reference material MBBA, we should have $1.0\leqslant\eta\leqslant 1.5$, which would produce a transition line slightly above the one for $\eta=0$, which line can be thought of as representative of a low-molecular-weight material with roughly equal elastic

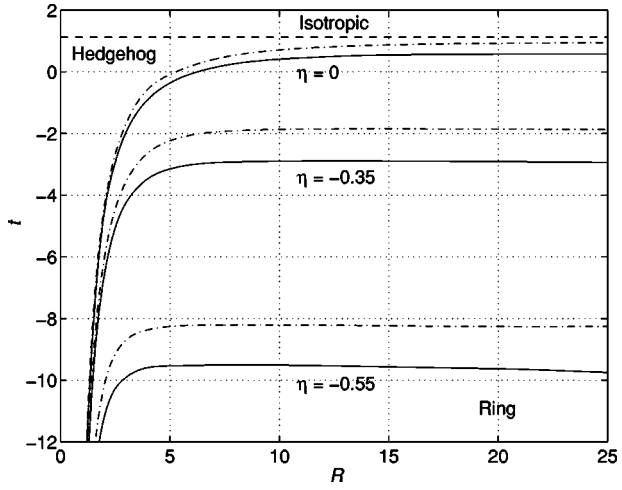

FIG. 9. Phase diagram with upper coexistence limits for solutions of discretized model for three different values of elastic-constant ratio $\eta=0,-0.35,-0.55$. Reduced temperature (t) vs droplet radius (R in units of ξ_0). Above the solid line, the radial hedgehog is stable (minimum free energy). Below this line, the ring configuration is the global free-energy minimizer. Above the dash-dotted line, the ring solution ceases to exist.

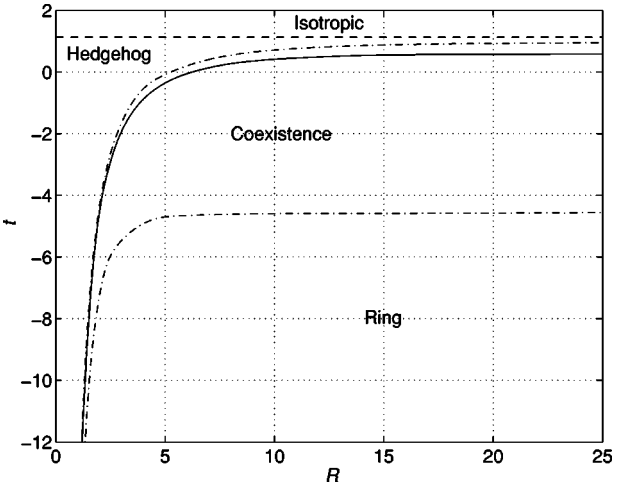

FIG. 10. Coexistence region for $\eta=0$ solutions of discretized model. Reduced temperature (t) vs droplet radius (R in units of ξ_0). Above the solid line, the radial hedgehog is stable (minimum free energy). Below this line, the ring configuration is the global free-energy minimizer. Above the higher dash-dotted line, the ring solution ceases to exist. Below the lower dash-dotted line, the hedgehog ceases to be metastable (locally stable).

constants—in such a case, the droplet radii R should be taken in units of 0.1 μm or so, and the temperatures t in °C below the pseudocritical temperature. The transition lines with $\eta<0$ would correspond to materials with $K_{22}>K_{11}=K_{33}$.

As observed in [3], for the equal-elastic-constants case, one obtains stable hedgehogs only for very small droplets ($R\lesssim 2-3$) or for high temperatures ($t\gtrsim 0.5$). Here now we can observe other features. First, the anisotropy in the elastic constants can significantly increase the stability region for the hedgehog [especially as the ratio $\eta=L_2/L_1$ approaches its limiting value of $-\frac{3}{5}$, as given in Eq. (1)], thus giving stable hedgehogs at much lower temperatures and in much larger droplets. Second, the coexistence region of the phases is rather large, of the order of five times the width of the coexistence region of the ordered and isotropic phases in the bulk. The split-core solution is always metastable; however, the ring solution (with the same parameters) always has lower free energy.

The lower limit of the coexistence region is given by the bifurcation point, the critical t or R value at which the hedgehog solution loses its metastability. It is difficult to locate these points with high accuracy in our numerical model, because of the imperfect bifurcation. We have approximated them by the horizontal-axis intercept of the line connecting the nearest points on the two (narrowly separated) branches.

Figure 7 corresponds to traversing in the vertical direction the $\eta=0$ phase-boundary line in the upper right corner of Fig. 10 (or Fig. 9); while Fig. 8 traverses this line in the horizontal direction in the lower left corner. The phase diagram in Fig. 9 also indicates how the bifurcation diagram (in Fig. 7) will change as η is changed: the whole picture shifts to lower temperatures as η is made more negative.

C. Equilibrium radius of ring configuration

In [2] Penzenstadler and Trebin perform a qualitative analysis to determine the equilibrium radius of the disclination ring. Their model differs from ours in two respects: they use a ball of infinite radius, and they impose the pointwise constraint (5) on the eigenvalues of the tensor order parameter. Their analysis is based on comparing the free energies for a certain ansatz for a hedgehog versus a ring. After minimizing with respect to the parameter controlling the radius of the disclination loop, they obtain a formula [Eq. (33) in their paper] for the equilibrium value, which in our units takes the form

$$\lambda_0 \simeq \sqrt{\frac{0.65+0.47\eta}{\sqrt[4]{-t}}}. \tag{6}$$

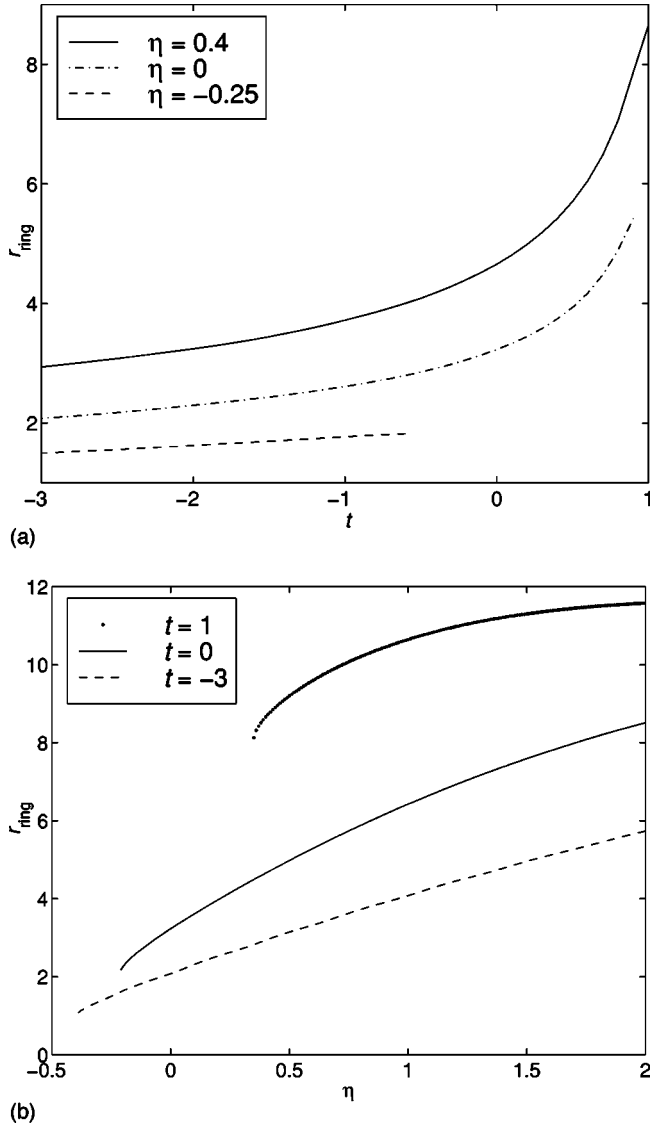

FIG. 11. Equilibrium radius of the ring configuration vs t (reduced temperature) for three different values of the elastic-constant ratio η (top), and vs η for three different values of t (bottom). Droplet radius $R=20$.

Figure 11 contains plots of the radius of the ring in our computed results versus t (for fixed η, top) and versus η (for fixed t, bottom). The trends and qualitative features are consistent with Eq. (6). We observe a very gradual decay in λ_0 as t is reduced and a fractional-power growth relative

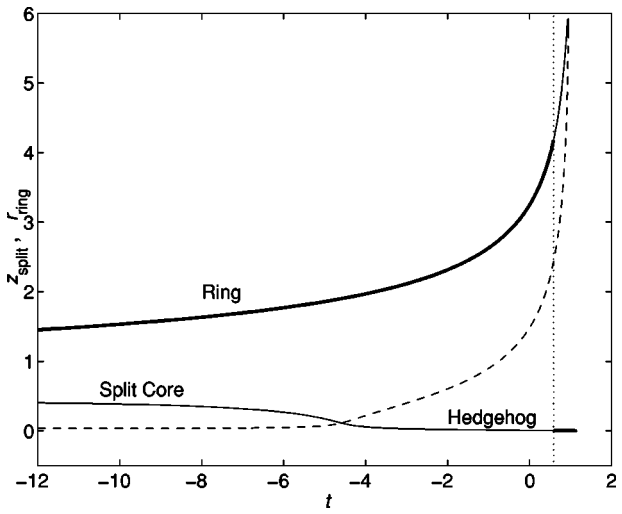

FIG. 12. Radius of ring (η_{ring}) and half length of split-core line disclination segment (z_{split}) vs reduced temperature (t). Bold line indicates stable equilibrium (minimum free energy); solid line indicates metastable (locally stable); dashed line indicates not metastable (not locally stable). Parameters: $\eta=0$, $R=25$. Transition value: $t\simeq 0.583$. Ring limit/turning point: $t\simeq 0.947$.

to η; although the divergence of λ_0 occurs as t approaches $\frac{9}{8}$, the superheating limit of the ordered phase in the bulk [as opposed to $t\to 0$, in Eq. (6) above]. Given the assumptions and approximations of the analysis in [2], we expect the quantitative agreement to be better for more negative values of t. For MBBA, with $1.0\leqslant\eta\leqslant 1.5$, the lower part of Fig. 11 indicates a ring radius of roughly $11\xi_0\approx 1.3\,\mu$m near the clearing point.

In comparison, the length of the line disclination of the split-core solution is shorter (than the radius of the ring) for moderate temperatures. It also appears to approach a limiting value of the order of a single unit of ξ_0 or less. See Fig. 12.

D. Degree of order and biaxiality

The pointwise constraint (5) utilized in the analysis of [2,4] in our units corresponds to

$$\mathrm{tr}(\mathbf{Q}^2)=-\frac{t}{2}.$$

Except for the vicinity of defects and disclinations, the tensor fields we compute are essentially uniaxial with degree of order equal to the bulk equilibrium value for that temperature:

$$\mathrm{tr}(\mathbf{Q}^2)\approx S_0^2=\left[\frac{3+\sqrt{9-8t}}{4}\right]^2=-\frac{t}{2}+O(\sqrt{-t})$$

as $t\to-\infty$. These values agree asymptotically (deep in the nematic phase); although they are not particularly close over the parameter ranges where we have done most of our computing—the rationale for Eq. (5) relies on $B^2\ll -24AC$, or $\frac{9}{8}\ll -t$ in our units.

Regarding the consideration of such a constraint in general, one can ask to what extent our calculated fields conform to (or deviate from) $\mathrm{tr}(\mathbf{Q}^2)=S_0^2$. A convenient parameter to gauge this is given by

$$\alpha^2:=1-\frac{\mathrm{tr}(\mathbf{Q}^2)}{S_0^2}, \tag{7}$$

which varies between 0 and 1, taking the value 0 when the order condition is exactly satisfied (as is the case in our outer boundary conditions, for example) and the value 1 when $\mathbf{Q}$ is zero (isotropic) and deviates maximally from the condition. We have plotted this in Figs. 13 and 14 for representative solutions of our three kinds, and we can see in these the localization of this quantity.

As well as coercing this degree of order, the bulk potential f_b penalizes configurations for departing from uniaxiality in general. Sometimes configurations do, however, ''escape'' to biaxiality, as we have seen above and has been demonstrated elsewhere. For such a model as ours, these regions of biaxiality are again localized to the vicinity of disclinations and such highly strained regions. To quantify and visualize this, we utilize the parameter

$$\beta^2:=1-6\,\frac{\mathrm{tr}(Q^3)^2}{\mathrm{tr}(Q^2)^3} \tag{8}$$

from [16] (which has been utilized for a similar purpose in [17]). As with α^2 above, this parameter takes values in [0,1], equals 0 if and only if $\mathbf{Q}$ is uniaxial, and 1 when it is ''maximally biaxial.'' We plot this for representative ring and split-core solutions in Figs. 13 and 14—the radial hedgehog is everywhere uniaxial.

We see that the departure from uniaxiality is very highly localized. Also, comparing the variations of β^2 with those of α^2, for both the ring and the split-core solutions, we can see the slightly shorter length scale of the escape to biaxiality (compared to the scale of variations of the degree of order), as this is determined by a ''biaxial coherence length'' [see [2], Eq. (14)]. Deeper in the nematic phase, we expect to see this situation reversed, since the biaxial coherence length scales like $1/\sqrt[4]{-t}$ (in our units); whereas the nematic correlation length (coherence length) scales like $1/\sqrt{-t}$.

V. CONCLUSIONS AND DISCUSSION

We summarize the main observations that have been made. The transition from the radial hedgehog configuration to the ring is first order and in fact rather strongly so (at least relative to the first-order nematic-isotropic transition in the bulk). The dependence of certain features on the elastic constants can be pronounced, and in particular the expanding of the stability and metastability regions of the hedgehog as the ratio L_2/L_1 becomes more negative is consistent with [4]. The equilibrium radius of the ring follows (at least qualitatively) the prediction of [2]; the ranges where we expect better quantitative agreement are for more negative values of t and are beyond the reach of our code. With respect to the constraint used in [2,4], we have found no instance where significant qualitative differences were caused by this; al-

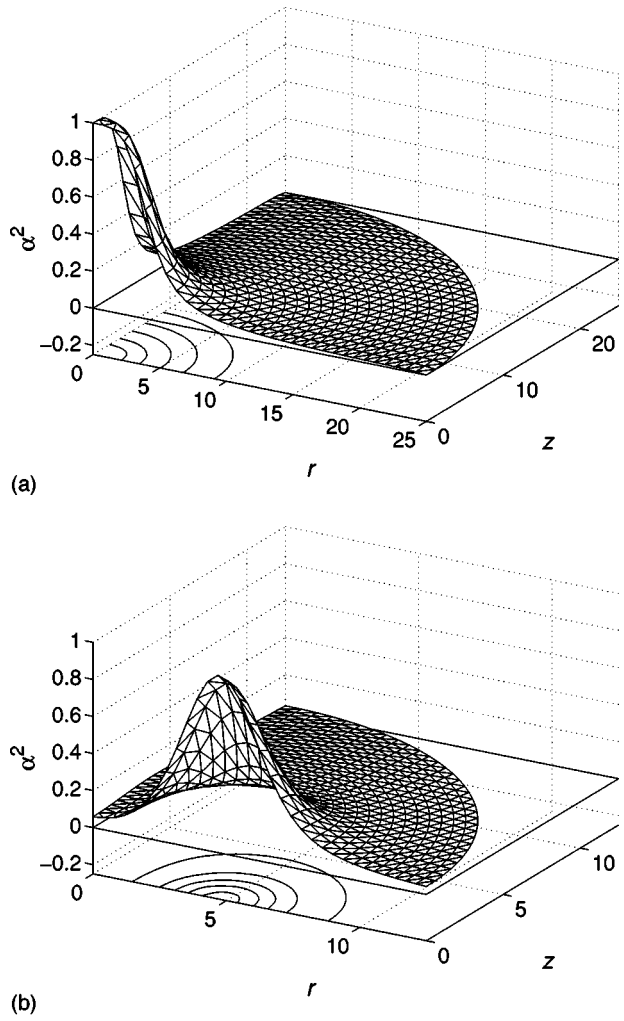

FIG. 13. Order condition parameter [α^2, Eq. (7)] for hedgehog (top) and ring (middle, inner region). Degree of biaxiality parameter [β^2, Eq. (8)] for ring (bottom, enlargement of local region). Parameters: $\eta=0$, $t=0.75$, $R=25$.

though quantitative agreement can be poor for the higher temperatures.

The split-core solution serves to complete the bifurcation picture. It is metastable in our symmetry class. We question whether or not it will remain metastable in a full three-dimensional calculation (in which axial symmetry is not imposed). There are some factors working against it. First, from an elastic point of view, the 360° disclination is an unfavorable configuration, usually stable only for very small capillaries and such [3,18]. Second, from the point of view of the bulk potential, we know that the negative-S potential well of f_b (in which the scalar order parameter of **Q** approximately lies for those points along the disclination line segment) is metastable in the bulk only under the restriction that **Q** be uniaxial (which is forced upon us here along the z axis by symmetry); the negative-S equilibrium is unstable in the bulk with respect to biaxial perturbations. It is possible that, once unshackled from the constraints of symmetry, the disclination line segment of the split-core configuration would broaden itself to a (vertically oriented) ring, as has been suggested to us [19].

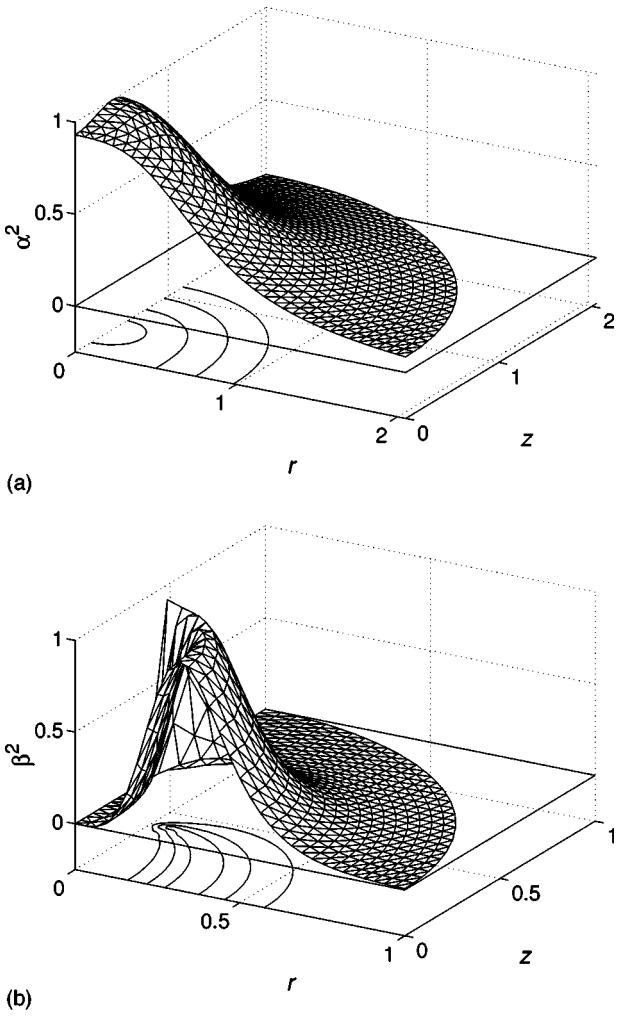

FIG. 14. Order condition parameter [α^2, Eq. (7), top] and degree of biaxiality parameter [β^2, Eq. (8), bottom] for split-core (line disclination segment) solution (enlargement of inner region). Parameters: $\eta=0$, $t=-12$, $R=25$.

One can contemplate ways to enhance the stability of the split-core solution. One possibility would be to apply a magnetic field using a material with a negative magnetic anisotropy—a positive anisotropy would likely only further discourage it. Another possibility would be to use elongated (ellipsoidal) droplets. In particular, if these droplets were very small (submicrometer size), then one would approach a situation similar to the (small) cylindrical capillary case,

mentioned above, where planar radial structures do indeed become stable. In fact, such configurations have been found in Monte Carlo simulations of such droplets, which are of interest in HPDLCs (holographically formed polymer dispersed liquid crystals) [20]. The effect of electric or magnetic fields on hedgehogs would also seem to depend on whether the material has a positive or negative dielectric or magnetic anisotropy. In the positive case, we would expect the field to encourage the ring configuration and broaden its radius; while we would anticipate the opposite to be true for a liquid crystal with a negative anisotropy.

We make two points of a more general nature. First, we advocate the type of full numerical bifurcation analysis done here, for investigations of this type in general. The more direct approach of numerically minimizing discretized free energies allows one to compute only metastable configurations; as we have seen here, the (locally) unstable solution branches connect the various branches and complete the picture, allowing one to delimit metastability regions and such. The packages we have used here are not equipped for automatic bifurcation analysis (path following, detection of bifurcation points, branch switching, etc.)—we could find no such package at the time—and so the information had to be put together in pieces. A public-domain package that does include full numerical bifurcation capabilities for scalar elliptic partial differential equations is PLTMG [21]. A package that came to our attention later is Cliffe's ENTWIFE code [22,23]. Commercial packages exist for other specialized applications, such as computational fluids, structural engineering, etc.

Second, phenomenological (order-parameter) models such as these Landau models are mesoscopic in nature. They are appropriate for the type of fine-scale analysis done here; they are not of use for truly macroscopic modeling, for example, of display devices. When they are nondimensionalized, one obtains a generic coupling of the form

$$\left(\frac{\xi}{d}\right)^2 \times (\text{elastic}) + (\text{bulk}),$$

where ξ is an intrinsic (molecular) length scale and d a geometric one. Thus for $d \gg \xi$ the problem is badly singularly perturbed. Moreover, in the ''outer limit'' (as $\xi/d \to 0$), the reduced problem is ill posed: only the bulk terms remain, $\mathbf{Q}$ is coerced to be uniaxial with the appropriate bulk equilibrium degree of order, but the orientation of the director is completely free. Thus for $d \gg \xi$ significantly different tensor fields can have nearly indistinguishable free energies (below discretization, numerical-resolution levels). This intrinsic mathematical ill conditioning severely challenges both asymptotic approaches (which require the piecing together of well-defined inner and outer solutions) and numerical approaches (based upon graded meshes and such).

As a final point, we emphasize that all of the structures we have explored here are very small in size, of the order of the core of the radial hedgehog [which scales like $\sqrt{(1+2\eta/3)/(-t)}$ in our units, see [1,15]]. For typical low-molecular-weight liquid crystals, it is not clear if these could ever be detected experimentally; for other materials (polymer liquid crystals, for example), it might be possible. There are other ringlike (and some line) structures in liquid-crystal droplets that have been observed experimentally, as well as analyzed theoretically and calculated numerically [24–29]. These are different structures, with a much larger radius ring (and overall droplet size and such) than those explored here. Some of these other systems also involve other aspects (such as external fields, weak surface anchoring, chirality, or negative dielectric anisotropy), and the analysis of them is usually in terms of the (macroscopic) Oseen-Frank elastic continuum theory. Because of the ill conditioning discussed above, we were unable to expand our domain to a size sufficient to capture one of these other, larger configurations. Much of the work reported here has been adapted from [30], where other aspects of this problem are also addressed.

ACKNOWLEDGMENTS

The authors are grateful to Professor Hans-Rainer Trebin (Stuttgart) and Professor Epifanio G. Virga (Pavia) for their encouragement in this project. We also gratefully acknowledge the input of Professor Oleg D. Lavrentovich and Professor Peter Palffy-Muhoray (Kent). We appreciate the help of the parallel ELLPACK group at Purdue (especially Professor John R. Rice, Professor Elias N. Houstis, Ann Christine Catlin, and Dr. Sanjiva Weerawarana) for prerelease versions of their software and for assistance in porting their package and the VECFEM library. This work was supported by the National Science Foundation under Grant Nos. DMR 89-20147 (ALCOM Center) and DMS-9870420 (E.C.G.).

APPENDIX A: FREE-ENERGY DENSITY IN CYLINDRICAL COORDINATES

For our application, we require the free-energy density in cylindrical coordinates and subject to the additional restriction that $\mathbf{Q}$ take the form (2). The needed expressions can be derived in various ways, for instance, by using the covariant tensor calculus. Alternatively, one can proceed directly from the Cartesian representation

$$\mathbf{Q}(r,\theta,z) = q_1(r,z)\mathbf{R}(\theta)\mathbf{E}_1\mathbf{R}(\theta)^T + q_2(r,z)\mathbf{R}(\theta)\mathbf{E}_2\mathbf{R}(\theta)^T + q_3(r,z)\mathbf{R}(\theta)\mathbf{E}_3\mathbf{R}(\theta)^T,$$

where $\mathbf{R}(\theta)$ is the rotation matrix

$$\mathbf{R}(\theta) = \begin{bmatrix} \cos\theta & -\sin\theta & 0 \\ \sin\theta & \cos\theta & 0 \\ 0 & 0 & 1 \end{bmatrix}.$$

A computer algebra system is very helpful, and for this we have utilized the MAPLE package. The following expressions are obtained (for general L_1, L_2, A, B, and C):

$$f_e = \frac{L_1}{2}\left[q_{1,r}^2 + q_{2,r}^2 + q_{3,r}^2 + q_{1,z}^2 + q_{2,z}^2 + q_{3,z}^2 + \frac{1}{r^2}(4q_2^2 + q_3^2) \right]$$
$$+ \frac{L_2}{2}\left[\frac{1}{6}(q_{1,r}^2 + 3q_{2,r}^2 + 3q_{3,r}^2 + 4q_{1,z}^2 + 3q_{3,z}^2) \right.$$
$$\left. + \frac{1}{\sqrt{3}}(-q_{1,r}q_{2,r} - q_{1,r}q_{3,z} + 2q_{1,z}q_{3,r} + \sqrt{3}q_{2,r}q_{3,r}) \right.$$

$$+\frac{1}{r}\left(-\frac{2}{\sqrt{3}}q_{1,r}q_2+\frac{2}{\sqrt{3}}q_{1,z}q_3+2q_2q_{2,r}+2q_2q_{3,z}+q_3q_{3,r}\right)+\frac{1}{2r^2}(4q_2^2+q_3^2)\Bigg]$$

and

$$f_b=\frac{A}{2}(q_1^2+q_2^2+q_3^2)-\frac{B}{3}\left(-\frac{\sqrt{6}}{2}q_1q_2^2+\frac{\sqrt{6}}{4}q_1q_3^2+\frac{3\sqrt{2}}{4}q_2q_3^2+\frac{\sqrt{6}}{6}q_1^3\right)+\frac{C}{4}(q_1^2+q_2^2+q_3^2)^2.$$

APPENDIX B: OUTER BOUNDARY CONDITIONS

The radial strong-anchoring condition (3) can be transformed into the following boundary conditions on the unknown scalar fields q_1, q_2, and q_3:

$$q_1(r,z)=\left(1-\frac{3r^2}{2R^2}\right)S_0,\quad q_2(r,z)=\frac{\sqrt{3}r^2}{2R^2}S_0,$$

and

$$q_3(r,z)=\frac{\sqrt{3}rz}{R^2}S_0\quad \text{on}\quad r^2+z^2=R^2.$$

[1] N. Schopohl and T. J. Sluckin, J. Phys. (France) **49**, 1097 (1988).
[2] E. Penzenstadler and H.-R. Trebin, J. Phys. (France) **50**, 1027 (1989).
[3] A. Sonnet, A. Kilian, and S. Hess, Phys. Rev. E **52**, 718 (1995).
[4] R. Rosso and E. G. Virga, J. Phys. A **29**, 4247 (1996).
[5] E. C. Gartland, Jr., P. Palffy-Muhoray, and R. S. Varga, Mol. Cryst. Liq. Cryst. **199**, 429 (1991).
[6] C. Chiccoli *et al.*, J. Phys. II **5**, 427 (1995).
[7] S. Chandrasekhar, *Liquid Crystals*, 2nd ed. (Cambridge University Press, Cambridge, 1992).
[8] L. Longa, D. Monselesan, and H.-R. Trebin, Liq. Cryst. **2**, 769 (1987).
[9] T. A. Davis and E. C. Gartland, Jr., SIAM (Soc. Ind. Appl. Math.) J. Numer. Anal. **35**, 336 (1998).
[10] E. N. Houstis, *et al.*, ACM Trans. Math. Softw. **24**, 30 (1998).
[11] L. Grosz, C. Roll, and W. Schönauer, in *Finite Element Methods, Fifty Years of the Courant Element*, edited by M. Krizek, P. Neittaanmaeaki, and R. Stenberg (Dekker, New York, 1994), pp. 225–234.
[12] http://www.cs.purdue.edu/research/cse/pellpack.html
[13] http://www.massey.ac.nz/~lgrosz/vecfem/
[14] P. G. Ciarlet, *The Finite Element Method for Elliptic Problems* (North-Holland, Amsterdam, 1978).
[15] E. C. Gartland, Jr. and S. Mkaddem, Phys. Rev. E **59**, 563 (1999).
[16] P. Kaiser, W. Wiese, and S. Hess, J. Non-Equilib. Thermodyn. **17**, 153 (1992).
[17] S. Kralj, E. Virga, and S. Žumer, Phys. Rev. E **60**, 1858 (1999).
[18] E. C. Gartland, Jr., Technical Report No. ICM-199511-03, Kent State University (unpublished).
[19] H.-R. Trebin (private communication).
[20] G. P. Crawford (private communication).
[21] R. E. Bank, PLTMG: *A Software Package for Solving Elliptic Partial Differential Equations: Users' Guide 8.0* (SIAM, Philadelphia, 1998).
[22] K. A. Cliffe, Technical Report No. AEAT-0823, AEA Technology, Harwell, Didcot, Oxfordshire, U.K. (unpublished).
[23] G. Blake, T. Mullin, and S. J. Tavener, Dyn. Stab. Syst. **14**, 299 (1999).
[24] O. D. Lavrentovich and E. M. Terentjev, Zh. Eksp. Teor. Fiz. **91**, 2084 (1986) [Sov. Phys. JETP **64**, 1237 (1986)].
[25] J. Erdmann, S. Žumer, and J. Doane, Phys. Rev. Lett. **64**, 1907 (1990).
[26] D. E. Yang and P. P. Crooker, Liq. Cryst. **9**, 245 (1991).
[27] S. Kralj and S. Žumer, Phys. Rev. A **45**, 2461 (1992).
[28] F. Xu, H. S. Kitzerow, and P. P. Crooker, Phys. Rev. A **46**, 6535 (1992).
[29] S. Komura, R. Atkin, M. Stern, and D. Dunmur, Liq. Cryst. **23**, 193 (1997).
[30] S. Mkaddem, Ph.D. thesis, Department of Mathematics and Computer Science, Kent State University, 1998.